JAAS

ROYAL SOCIETY OF CHEMISTRY

PAPER

View Article Online
View Journal | View Issue

Cite this: *J. Anal. At. Spectrom.*, 2025, **40**, 808

Plasma evolution investigation and aging grade evaluation of heat resistant steel based on laser induced plasma images†

Junbin Cai,[ac] Meirong Dong,[*ac] Feiqiang Tang,[ac] Kaiqing Chen,[ac] Zhichun Li,[ac] Weijie Li,[b] Shunchun Yao[ac] and Jidong Lu[ac]

The accurate evaluation of heat-resistant steel deterioration using laser-induced breakdown spectroscopy (LIBS) is of great importance for the safe operation of high-temperature pressure equipment. Understanding how plasma expresses matrix properties and utilizing plasma information effectively can lead to achieving more effective detection methods. In this study, the plasma evolution and pulse fluctuations of typical heat-resistant steel T91 are studied based on plasma images to understand the different evolution stages and characteristics of plasma. T91 specimens with different aging grades are employed to investigate the expression form, evolution and identification of matrix information on plasma. Subsequently, the plasma images and the RSD images based on pulse–pulse relative standard deviation (RSD) were employed to build an aging grade evaluation model, the best model accuracies were 96.6% and 96.0%, respectively. A model combining these two image features achieved the highest accuracy at 99.8%. Finally, the effects of the delay time, region selection, and data coupling strategy on model performance were explored. The results indicate that the temporal–spatial characteristics, identification, and stability of plasma information have a significant effect on the performance of the model. This study deepens the understanding of the plasma evolution and matrix effect of heat-resistant steel and expands the application of plasma image information for property detection.

Received 16th October 2024
Accepted 17th January 2025

DOI: 10.1039/d4ja00368c

rsc.li/jaas

1. Introduction

High-temperature pressure equipment is widely used in electric power generation, metallurgy, power machinery, petrochemical and other industries. The metal heating surfaces of the equipment are used long-term under harsh working conditions. High temperature, high pressure, wear and corrosion contribute to metal deterioration. Aging of heat-resistant steel is mainly caused by changes in the metallographic structure. The microstructure and element distribution in steel undergo irreversible changes. Over time, this directly leads to a decrease in the mechanical properties of the material, ultimately resulting in the inability of the steel to operate under service conditions, and the risks of leakage and explosion gradually increase. Therefore, accurately detecting the failure trends and service status of metal materials on the heating surface can minimize unplanned equipment outages and enhance the operational reliability and economy of equipment. However, traditional detection methods are destructive and time-consuming. LIBS has the capability to rapidly test material properties without causing damage. It also avoids the limitations of existing non-destructive testing technologies such as detection damage type constraints, challenging working environments, and possible health hazards. In addition, LIBS can be integrated into portable or remote online measurement equipment and can even serve as the basis for building metal heating surface detection and tracking management systems.[1,2]

Our research team has conducted a series of studies on LIBS detection applications for heat-resistant steel. Firstly, the plasma and spectral characteristics of typical heating surface materials with different damage states or microstructures were studied.[3,4] Linear relationships between specific characteristic spectral line intensities, intensity ratios, or plasma characteristic parameters and metal hardness,[5] grain size grade,[6] or aging grade[7] were discovered. The plasma and spectral information under the influence of matrix effects were determined to be potential indicators for evaluating matrix properties. Subsequently, we carried out research on ablation adjustment, signal acquisition, data optimization, and modeling schemes. Lu *et al.*[8] studied the effect of continuous laser ablation and sampling setting on spectral data quality and model

[a]*School of Electric Power Engineering, South China University of Technology, No. 381 Wushan Road, Tianhe District, Guangzhou, Guangdong, 510640, P. R. China. E-mail: epdongmr@scut.edu.cn; jidlu@scut.edu.cn*

[b]*School of Environmental Science and Engineering, Hubei Polytechnic University, Huangshi, Hubei, 435003, P. R. China*

[c]*Guangdong Province Engineering Research Center of High Efficient and Low Pollution, Guangzhou, Guangdong, 510640, P. R. China*

† Electronic supplementary information (ESI) available. See DOI: https://doi.org/10.1039/d4ja00368c

performance. Huang *et al.*[9,10] analyzed the spectral noise and multicollinearity of spectral variables and tried to optimize the spectral data by denoising and reducing dimensionality. Further, they employed different feature selection methods such as K-fold-support vector machine-recursive feature elimination (K-SVM-RFE) and layered interval wrapper (LIW) to select input spectral variables for modeling, improving the model efficiency, accuracy, and robustness.[10,11]

Recent research has developed portable LIBS devices for heat-resistant steel detection and attempted to solve problems such as insufficient detection performance of portable devices and interference from the surface layer of heat-resistant steel. Shang *et al.*[12] used the Lorentz function to correct spectral peaks and optimized the spectral signal by introducing a Kalman filter, enhancing the accuracy and stability of portable devices. Zhang *et al.*[13,14] and Cai *et al.*[15] combined spectral correction and screening to reduce the interference of the metal surface layer and achieved the evaluation of actual service heat-resistant steel by using artificial sample models.

In order to deeply understand the mechanism of steel degradation measurements, Lu *et al.*[16] investigated the temporal–spatial evolution of spectra of T91 steel specimens with different aging grades by using a grating spectrometer with an intensified charge-coupled device detector (ICCD). The correlation between the ionic and atomic spectral lines as well as the plasma temperature and the aging grade in specific time and space were found. In addition, the analysis of the ablated craters based on three-dimensional surface topographies found that the crater volume is proportional to the aging grade.

Plasma imaging is also an effective way to study the plasma evolution and matrix effect mechanism. Image information is an intuitive visual representation of plasma and a convenient way to obtain and analyze the characteristics of plasma evolution. Wang *et al.*[17] studied the characteristics of plasma images at different delay times and the stability of different pulse images. They investigated the transition process of plasma from stable to unstable, thereby discovering the distortion phenomenon that occurs in the early stages of plasma. Zhao *et al.*[18,19] employed plasma images to study the temporal–spatial species distribution and dynamics of plasma from a binary miscible alloy and a binary immiscible alloy. Ding *et al.*[20] investigated the temporal–spatial evolution of plasma under orthogonal ablation and oblique ablation based on a fast plasma imaging method.

In addition, image information is also used by some scholars for information compensation and detection optimization. Schechter *et al.*[21] proposed that plasma images are valuable references for signal correction, and the temporal and spatial characteristics of the images can be used for detection parameter setting confirmation, matrix effect compensation, and even as an alternative to a time-gated detector. Ni *et al.*[22] developed a normalization method based on the integrated intensity of plasma images to reduce the influence of the experimental parameter fluctuation. Zhang *et al.*[23] utilized plasma images to overcome the spectral fluctuation caused by different sample surface heights. Li *et al.*[24] used the intensity and morphology of plasma images to standardize the spectrum, reducing the influence of plasma pulse fluctuation on detection in water. Zhang *et al.*[25] employed the plasma images as a reference for the degree of self-absorption and optimized the quantitative analysis. Guo *et al.*[26] found that the change of ablation crater morphology can be well reflected in the plasma image, so the three-dimensional distribution analysis of surface elements can be achieved based on this reflection. They also extracted brightness and area information from plasma images, respectively characterizing plasma temperature and ablation quality to correct matrix effects.[27] Recently, they proposed spectral standardization[28] and screening[29] methods based on image information and also innovated image-based plasma parameter inversion and correction schemes to optimize the detection performance.[30–32]

To date, the temporal–spatial plasma evolution and matrix effects of heat-resistant steel based on plasma images have not been explored. Now we have a better understanding of plasma evolution, especially after the early unstable distortion of plasma was discovered. The expression of matrix properties on heat-resistant steel plasma can advance from the phase of spectral or plasma parameter research toward gaining a deeper understanding through image-based analysis of plasma morphology evolution. In addition, the current detection methods of heat-resistant steel mainly rely on spectroscopy and are optimized by imitating the LIBS quantitative analysis method. A thorough properties evaluation scheme should be developed based on the understanding of the expression mechanism of the matrix by plasma, and the plasma image information should be better used.

Therefore, this study investigated the plasma evolution process of heat-resistant steel based on plasma images. We explored the plasma expression of the matrix effect and its temporal–spatial characteristics. We also attempted to employ plasma image features for aging grade evaluation and performed spatial region selection, denoising, and image feature fusion. Finally, based on the understanding of the mechanism of matrix manifestation on plasma, the performance variation of image-based models was discussed.

2. Experimental

2.1 LIBS setup

The schematic diagram of the LIBS experimental system is shown in Fig. 1. The laser source is a Q-switched Nd:YAG laser (EaZy, Quantel) operated at 1064 nm with 6 ns pulse duration.

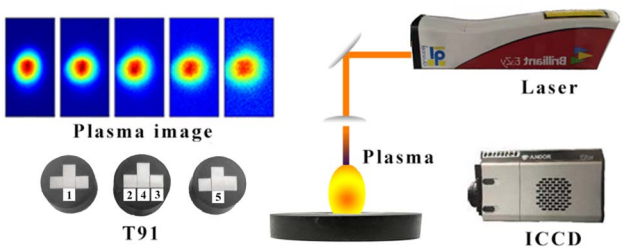

Fig. 1 A schematic diagram of the LIBS experimental system.

The laser incidence direction is perpendicular to the specimen surface, and the focal point is set to 2 mm below the surface to minimize air breakdown. The laser pulse energy was adjusted to 45 mJ and the repetition rate was set to 2 Hz. An intensified charge-coupled device (ICCD, DH734, Andor) detector (1024 × 1024 pixels) was arranged parallel to the specimen surface to capture plasma images. The aim was to obtain clear images of different stages of plasma evolution. The delay time between laser triggering and image acquisition was set to 50 ns, 100 ns, 150 ns, 200 ns, 400 ns, 600 ns, 800 ns and 1000 ns. The detection gate widths are uniformly set to 50 ns and ablation is performed 3 times under each parameter setting, obtaining 40 images each time.

2.2 Specimens

Typical heat-resistant steel T91 was employed as the research object. The specimens with different aging grades were obtained by heat treatment. The preparation details of the artificial aging specimens have been described in our previous work.[7–11] In terms of the metallography inspection and assessment standard, the specimens were graded into 1–5 grades as shown in Fig. 1.[33,34]

2.3 Methods

2.3.1 Linear discriminant analysis (LDA). Linear discriminant analysis (LDA) was proposed by Fisher in 1936.[35] The basic principle of LDA is to minimize the variance of intra-class data and maximize the variance of inter-class data in the projection transformation of data. It is a supervised learning algorithm that requires knowledge of the classification of the training set data. The calculation formula is as follows:

$$y^* = \frac{n_0 m_0 + n_1 m_1}{n_0 + n_1} \quad (1)$$

where m_0 and m_1 correspond to the class mean of the projected samples, n_i represents the sample size of the i^{th} class sample. Classification is performed based on decision rules. When $y > y^*$, the test sample belongs to L_0, otherwise, it belongs to L_1.

3. Result and discussion

3.1 Plasma evolution and expression of matrix

In order to investigate the plasma evolution of T91 steel, plasma images at different delay times were studied. Fig. 2a shows the plasma image of a typical T91 steel within 50–1000 ns (aging grade 1). In order to observe the evolution of plasma morphology more clearly, the image brightness values at each delay time were normalized to 0–1 separately. It was found that there was no significant change in plasma volume during the first two delay times, while compared to the elliptical structure along the laser propagation direction presented at 50 ns, the plasma at 100 ns is closer to a circular shape. At 100–200 ns, the plasma mainly undergoes longitudinal expansion, and the overall volume gradually increases. Then the lateral expansion is comparable to its longitudinal expansion after 400 ns. The shape of the plasma changes from an ellipse to an incompletely regular circle.

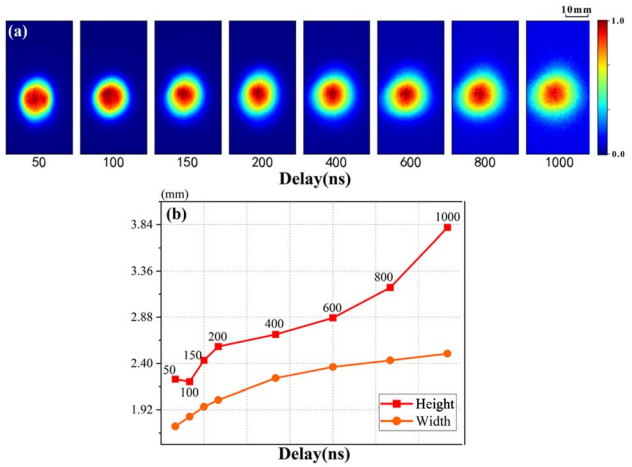

Fig. 2 (a) Typical plasma image; (b) the mean values of plasma height and width within 50–1000 ns.

The morphology of plasma at different stages can be further analyzed based on temporally-resolved plasma height and width. The height and width in Fig. 2b are the mean values of plasma for all T91 specimens. The calculation threshold for the plasma boundary is 5% of the highest emission intensity at each delay time. Based on this floating threshold, the spatial characteristic of the main emission region of the plasma can be clearly observed. As can be seen from the figure, the variation of plasma height clearly presents a decreasing trend at 100 ns. Combined with the above image analysis, it can be determined that the plasma distortion process in the early life of plasma occurs. This is an important stage in plasma evolution, which occurs due to the interaction between the primary plasma and the environmental medium. The transfer of energy and momentum occurs during the interaction process, and a shock wave is generated at a specific moment. The frontier of the plasma is subjected to the reaction of the shock wave, which is manifested as the frontier component migrating downward and crashing into the middle and lower parts.[17] The plasma is in its initial state of propagation at 50 ns, and the plasma height is relatively small. Then the occurrence of plasma distortion at 100 ns further reduces the height. In the following 100 ns, the plasma undergoes the highest rate of expansion in its lifetime. After 400 ns, the longitudinal expansion rate of the plasma slows down.

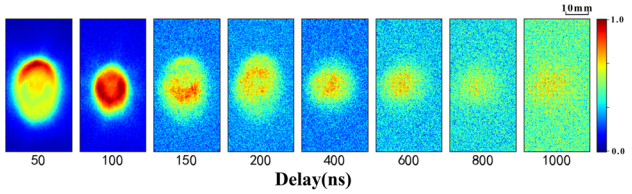

Fig. 3 Typical plasma RSD image of T91 steel within 50–1000 ns.

In order to analyze the disturbance caused by the distortion, the RSD of emission intensity for each pixel under 120 pulses is investigated and shown in Fig. 3 (aging grade 1). Similarly, to better observe the evolution of emission fluctuation, the brightness values at each delay time are normalized separately. The bright area of the RSD distribution map at 50 ns shows a significantly larger volume compared to the plasma image, which is caused by fluctuations in the spatial distribution and peripheral emission of the strong initial plasma. In addition, due to the randomness of the upward propagation of initial plasma and its interaction with the environment. The region with the highest RSD value is located in the plasma frontier. At 100 ns, the bright area significantly decreases and is close to the volume of the plasma. The high RSD value area is located in the middle and lower parts of the plasma. Due to the plasma distortion, the impact of the sinking component on the middle and lower parts of the plasma increases the emission fluctuation. At 150 ns, the volume of the bright area increases, while the high-value area still tends to be located in the middle and lower parts of the plasma. Then this tendency disappears at 200 ns. During 100–200 ns, the bright area is similar to the plasma volume, indicating that the main reason for the fluctuation is the difference in emission distribution within the plasma plume, rather than the overall spatial position shift of the plasma. In the subsequent delay time, the bright region becomes smaller while the plasma volume continuously increases, indicating that the fluctuation mainly occurs in the plasma core. Moreover, at this stage, it can be seen that the fluctuations in plasma emission are significantly reduced and gradually reach similar values to background noise. Therefore, the evolution of plasma within 50–1000 ns can be roughly described as four stages: initial plasma (50 ns), plasma distortion (100 ns), transition state after plasma distortion (100–400 ns) and subsequent propagation of plasma (400 ns).

In these different plasma stages, the similarities of the plasma emission distribution between different pulses will also undergo large changes. In order to analyze and compare the similarity of emission distribution, the correlation coefficient of the plasma images was calculated. The correlation coefficient is calculated by taking the column vectors at the same position in the different images, respectively. The mean correlation coefficients of all column vectors in the figure are the correlation coefficients of the images. As shown in Fig. 4a, the correlation coefficient of the plasma images between different laser pulses is inversely proportional to the delay time. When the initial plasma stage evolves into the distortion stage, the correlation coefficient remains at a high value and does not show a significant decrease, indicating that the plasma at this stage is less sensitive to pulse fluctuations. However, the correlation coefficient rapidly decreases at 100–200 ns because the plasma distortion amplifies the slight differences in the initial plasma caused by Rayleigh–Taylor instability (RTI),[36,37] surface roughness and possible substrate unevenness. The plasma undergoes a process of transition from stable to unstable. In order to further analyze the influence of distortion on plasma evolution, the correlation coefficient of plasma images between different times are investigated. Fig. 4b shows the correlation coefficients between the plasma image at each delay time and the stages at 50 ns, 100 ns, 150 ns and the previous delay, respectively. These time periods represent the initial state, distorted state, re-expansion after distortion and the evolution of the previous moment of the plasma. It can be clearly found that the plasma images after 200 ns achieve the highest correlation coefficient with the state at 150 ns. In other words, the state of re-expansion after distortion determines the subsequent evolution. This moment could even be called the rebirth of the plasma.

For the purpose of matrix effect research, it is necessary to determine the expression form of matrix properties by plasma at different stages. Fig. 5 summarizes the average plasma characteristic parameters of the initial state and the re-expansion state after distortion. In order to compare each parameter more clearly, the normalization process is carried out respectively. It can be found that the emission intensity and volume of plasma have a negative correlation with the aging grade except for the specimen with aging grade 5. In the recent research results, it has been found that the volume of the ablative crater is proportional to the aging grade under the same ablation parameters.[16] Namely, the evaporated component decreases with the aging grade, and more laser energy acts on the excitation, so a bigger plasma with higher emission intensity is produced from the T91 with a lower aging grade. The anomaly of aging grade 5 may be related to the evaporate rate of the ablated species being high enough and reaching a special threshold. As is well known, the excitation stage can be divided into a pre-breakdown stage and a plasma forming stage. When the density of free electrons accumulates to a certain extent in

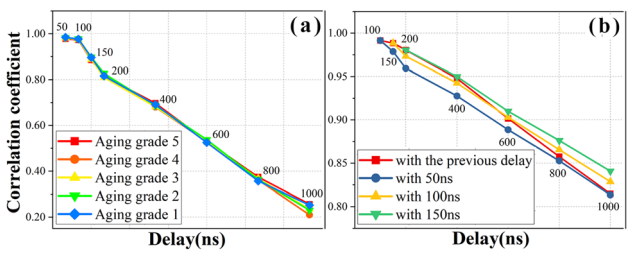

Fig. 4 (a) Plasma image correlation coefficients between different pulses; (b) plasma image correlation coefficients between different delay times.

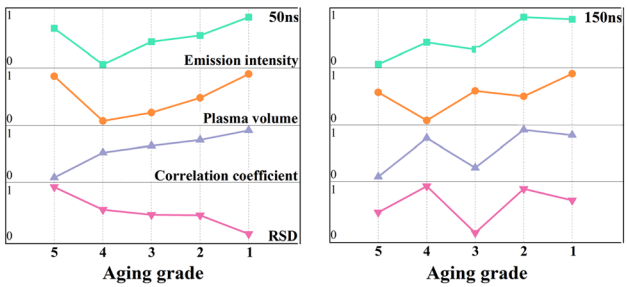

Fig. 5 Comparison of the plasma parameters of T91 steel with different aging grades.

the laser action area, avalanche ionization occurs and plasma is formed. The aging grade 5 specimen evaporating more species at a higher rate may accelerate the arrival of this moment. The plasma formed earlier absorbed more laser trailing edge energy, taking up a part of the energy that would otherwise pass through the plasma to the ablative region on the specimen surface. A comparison of the plasma center height of the aging grade 5 specimen with other specimens also fits with this hypothesis. The height of the plasma core from the sample surface of the aging grade 5 specimen (21.7 mm) is significantly lower than that of the other 4 specimens (25–28 mm), indicating that the evaporated component forms initial plasma earlier in the process of propagating towards the laser incidence direction. This is only one possible explanation, but these plasma parameters do show a near linear relationship with the aging grade. For the emission RSD and correlation coefficient, the increase in ablative evaporation enhances the interaction of components, and the distribution of excited species and the overall excitation effect are more random. Therefore, the correlation coefficient and RSD are negatively and positively correlated with the aging grade, respectively. However, in the stage of re-expansion after distortion (150 ns), these relationships have been basically disrupted.

It is obvious that the initial plasma is a stage in which the matrix characteristic information can be better reflected visually, and the plasma parameters are linearly or nearly linearly correlated with the matrix properties. The occurrence of distortion disrupts this correlation and seems to affect the characterization of matrix properties by plasma information. However, the identification degree of plasma characteristic information to the matrix cannot be judged only based on whether there is linear correlation, and its effectiveness should also undergo stability evaluation. Fig. 6a shows the difference in plasma correlation coefficient and RSD between the same specimen and different specimens. For example, the correlation coefficient of the same specimen is calculated based on data from the same sample under different pulses, while the correlation coefficient of different specimens refers to the average value calculated from each specimen compared to the other four specimens. Such a difference may represent the recognition of image features to the matrix to some extent. As shown in the figure, the overall trend is that the identification degree decreases with the delay time. Therefore, the time found in the above research that the plasma parameters have a near linear relationship is also the time point with the best matrix identification. However, as shown in Fig. 6b, the variation of emission RSD shows that this delay time is also the time point with the highest fluctuation of emission.

In a word, this section analyzed the plasma evolution and fluctuation and discovered the expression form and temporal evolution of the matrix message. To further investigate the expression effect and even attempt to apply plasma image information to matrix classification, the aging grade evaluation model based on plasma image features will be established in subsequent studies.

3.2 Modeling based on image features

Current property evaluation research is mainly based on plasma spectra. Actually, with continuous research into LIBS and the development of plasma information acquisition equipment, more and more plasma information is being investigated, including sound,[38] ablating crater,[39] and images. The linear relationship between image features and aging grade may be difficult to discover, but its representation of the matrix is deterministic. To verify the effectiveness of image information, the two-dimensional image matrix is firstly performed by matrix rank conversion into a one-dimensional matrix without preprocessing such as signal optimization or feature selection. Then a commonly-used LDA method was selected for modeling and to attempt to achieve aging grade evaluation. LDA is a simple and mature classification method. The calculation process is relatively simple and has strong interpretability. Compared to advanced complex algorithms, LDA can better demonstrate the validity of data.

Fig. 7 shows the evaluation accuracy of the model based on images at different delay times. In order to demonstrate that images are valuable and sensitive information related to the matrix, we deliberately increased the difficulty of modeling and only 20 pulses of data were employed as the training set for each specimen. The remaining 100 pulses of data served as a test set. The total sample numbers for the training set and the test set were 100 and 500, respectively. In addition to inputting the entire image, images of different regions were also employed to establish the model separately. The plasma is evenly divided into region 1 (lower), region 2 (middle), and region 3 (upper). In the case of inputting the entire image, the best accuracy reaches

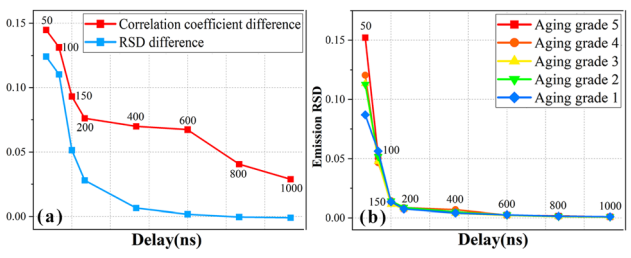

Fig. 6 (a) Difference in plasma correlation coefficient and RSD between the same specimen and different specimens; (b) emission RSD of T91 steel with different aging grades within 50–1000 ns.

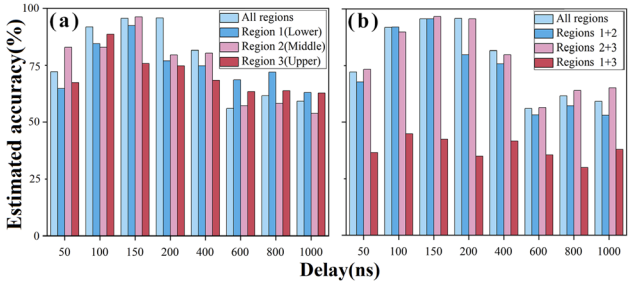

Fig. 7 Evaluation accuracy of aging grade models based on plasma images from different regions.

95.6% at 150 ns, which is the transition time period after plasma distortion. In most delay times, this model performs better than models based on single region information input (Fig. 7a). For models that combine different regions of plasma (Fig. 7b), the model based on the data of the middle and upper parts achieves the best accuracy at 96.6%. The best delay time is also 150 ns. The difference in the matrix induces a difference in the plasma distortion effects, and the image information in the middle and upper parts of the plasma, which is the key area of distortion, can better characterize the matrix under this modeling setting.

The above study also found that the fluctuations of plasma emission are significantly correlated with the matrix. More specifically, the differences in the matrix affect the plasma morphology, component distribution, and plasma–environment interaction. Plasma morphology refers to the region where the plasma mainly emits radiation, and radiation fluctuation between different pulses mainly occurs within this region. The component distribution directly affects the spatial distribution of radiation, and the interaction between the components emitting radiation and the interaction between the components and the environment also vary, which will be reflected in the radiation fluctuation between different pulses. As shown in the RSD distribution image of different specimens at 50 ns (Fig. 8), the volume of the area with a high RSD value (red) shows a nearly positive correlation with the aging grade. The difference in the matrix also induces visible differences in the plasma fluctuation. Such a feature may be of equal value or complementary to the plasma image. To verify the validity of RSD information, modeling based on RSD images was carried out. During this modeling process, four laser pulse images were used to obtain one RSD image. For each specimen, 20 RSD images obtained from 80 pulses were used as the training set, while 10 RSD images obtained from another 40 pulses were used as the test set. The modeling results indicate that the accuracy of the RSD model is approximately inversely proportional to the delay time. At 50 ns, the model achieves the highest accuracy, which is the time when a significant RSD distribution related to the matrix is discovered. Under different data selection modeling configurations, the highest accuracy reach 74% (the image is included in the ESI†). However, the accuracy is still far lower than modeling based on images.

In order to investigate the reason for the poor performance of the RSD model, the stability of the RSD data was first analyzed. Fig. 9a shows 5 randomly selected RSD images each

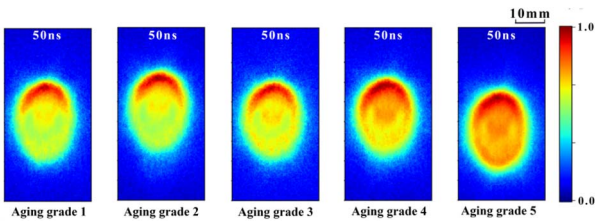

Fig. 8 Average plasma RSD images of T91 steel with different aging grades at 50 ns.

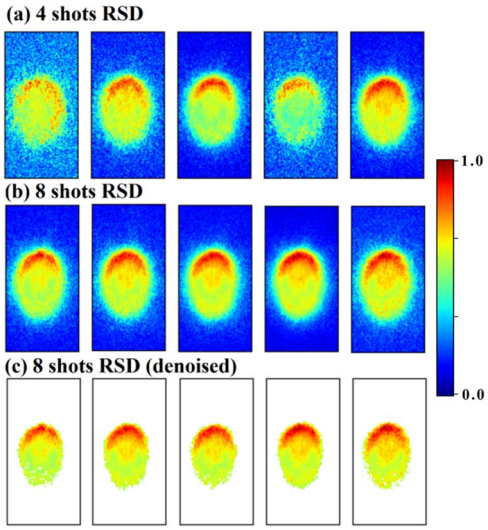

Fig. 9 Typical plasma RSD images calculated from (a) 4 shots, (b) 8 shots, and (c) 8 shots (denoised) at 50 ns.

calculated based on 4 plasma images. Although the images exhibit a similar pattern overall, their fluctuation is significant. This may be related to the number of data used to calculate RSD. Therefore, an attempt is made to use 8 plasma images to calculate RSD. Five randomly selected RSD images calculated from the data of 8 plasma images are shown in Fig. 9b. The fluctuation of data is significantly reduced, and the distribution of RSD value in different spatial locations of each image is more similar. The model built based on the RSD data obtained from 8 plasma images also achieves better performance. The best accuracy reaches 76% (the image is included in the ESI†).

In practical applications, when RSD is employed as a fingerprint for matrix evaluation, there will be a competition between data quality and acquisition efficiency. Calculations based on a larger amount of plasma image data can obtain better RSD data, but will also reduce the sample number of data sets concurrently. Moreover, when utilizing 8 shots RSD, although the stability of the RSD data has been improved, the current application is very poor compared with the direct application of the plasma image. Blindly increasing the amount of data used in RSD calculation is not advisable. For RSD, a commonly used parameter to evaluate data stability in detection, there are still many problems that need to be addressed when it is employed as a fingerprint of a matrix. The most important thing is to understand how RSD achieves matrix characterization. In the process of detection, fluctuations in the equipment operating state and environmental parameters always exist, so that the plasma changes randomly, but the different matrices intervene or even amplify these fluctuations. Therefore, RSD can characterize the matrix property, but RSD that are not affected by the matrix are useless, and certain measures should be taken to weaken or even solve the useless RSD. At the same time, the signal strength of RSD information should also be considered simultaneously. In fact, the changes in plasma morphology and component distribution caused by matrix differences can be

effectively reflected in the radiation fluctuations in the main radiation region of the plasma. Because of the high radiation intensity in this region, randomness between pulses eventually causes more pronounced fluctuation. The plasma edge is the key region of the interaction between plasma and environment, but the plasma radiation intensity in this region is low, and the quality of the generated RSD signal may be relatively poor. For regions away from the plasma, mostly ambient noise, these unwanted RSD values are relatively small and stable. Therefore, by removing the low-value RSD information with an appropriate threshold, a large number of useless RSD can be removed and beneficial RSD can be retained.

In order to obtain the optimal denoising threshold, data points were removed with 0.1–0.9 as the threshold, respectively. Fig. 10a shows the performance of the model with different thresholds at 50 ns. The highest accuracy is achieved when 0.5 is adopted as the denoising threshold, reaching 96%. Fig. 9c shows the RSD image after denoising. The non-plasma region fluctuations and weak plasma edge fluctuations are removed during the denoising process. It is known that these two kinds of fluctuation have a negative effect on matrix identification.

Furthermore, the denoised RSD image is combined with the plasma image to establish a stronger model. In the process of combination, the image corresponds to the RSD which it participates in calculating. For data integration modeling, different choices of information input have different effects. Different combinations were attempted. As shown in Fig. 10b, coupling the upper part of the RSD image with the middle and lower parts of the plasma image achieves the best accuracy at 150 ns. The accuracy of 99.8% is higher than the image model and RSD model. This selection scheme results in a good complementarity of two plasma image features.

3.3 Model performance variation analysis

The above study attempted to establish an aging grade model for heat-resistant steel based on two types of image features, both of which achieved high accuracy. However, the model characteristics of the two types of image features are different. The image model achieves the highest classification accuracy at 150 ns, while the model based on RSD achieves the highest accuracy at 50 ns. This is closely related to the evolution of plasma and its information, and the underlying mechanism will be analyzed below.

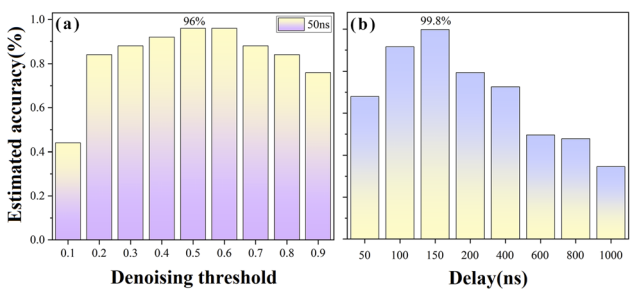

Fig. 10 (a) Evaluation accuracy of aging grade models based on 8 shots RSD with different denoising thresholds at 50 ns; (b) evaluation accuracy of the best image and RSD coupling models within 50–1000 ns.

In most cases, the greater the data difference between different samples, the more beneficial it is for the algorithm model to effectively classify them. As shown in Fig. 6a, the maximum identification of the matrix by RSD occurs at 50 ns and rapidly decreases with increasing delay time. This is similar to the variation of RSD model performance. The ablation mass, component propagation, and shock wave velocity change caused by the matrix result in a difference in the generation of plasma and its initial interaction with the environment. The higher energy and momentum level of the initial plasma make the RSD determined by the matrix more pronounced, thus forming an effective characterization of the matrix. But as the plasma distortion process occurs at around 100 ns and the overall energy level of the plasma gradually decreases, the characterization ability of RSD on the matrix gradually weakens.

For the image, the difference in the correlation coefficient also reaches its maximum at 50 ns. However, the optimal performance of the image model is achieved at 150 ns. Fig. 6b shows the time-resolved plasma emission intensity RSD. The RSD of emission intensity remains at a relatively high level at 50 ns and 100 ns. For the image, the fluctuation of the image is negative for the learning and testing of the model. Although there are more significant differences in the image among different specimens at smaller delay times, and some plasma parameters show linear and near-linear correlation with the aging grade, it is not the optimal parameter selection for model performance. After 100 ns, although the plasma distortion process slightly disturbs the linear relationship, the emission fluctuation has been significantly reduced. Taking all these factors into account, at 150 ns, the plasma image has lower fluctuation, as well as sufficient inter-group difference and emission intensity, so its model accuracy reaches the highest level.

In the case of spatial selection, different image features in different regions exhibit different modeling values. The plasma still experienced the influence of the sinking of the frontier component of the plasma at 150 ns, so the upper and middle regions of the plasma are effective regions for exhibiting matrix differences. The model based on the upper and middle region image achieves an outstanding performance. At 50 ns, the more beneficial RSD information is mainly located at the plasma frontier. The optimal region for the RSD model is the upper part of the plasma. In the data integration modeling, the complementarity of different image features should also be considered when selecting favorable regions. In the optimal data combination scheme, the RSD in the upper region and the plasma image in the middle and lower regions effectively characterize the matrix while containing information about the entire region of the plasma, avoiding information clutter, and achieving the highest classification accuracy.

4. Conclusions

This paper focuses on the plasma evolution process of heat-resistant steel, the expression of the matrix properties by

plasma, and the aging grade evaluation based on plasma image features. The results show that plasma evolution can be divided into four stages: the initial plasma, the distortion process, the transition period after the distortion, and the subsequent evolution. The emission fluctuation between pulses at different spatial positions is obviously related to the evolution stage. In the initial stage, the plasma characteristic parameters exhibit a near linear correlation with the aging grade, but the following distortion affects this correlation. The identification of the matrix properties using plasma image features also decreases with increasing delay time. However, plasma emission fluctuation is more intense at an earlier delay time. To further evaluate the value of this plasma information, plasma image features were used to establish aging evaluation models. By adopting an appropriate delay selection, region selection, and denoising process, models based on images and RSD could achieve accuracies of 96.6% and 96.0%, respectively. When the plasma image and RSD image are used together, the accuracy could be further improved to 99.8%. Based on the model performance variation, plasma evolution, and matrix expression, it was found that the plasma images in the stage after distortion and the regions mainly affected by distortion could better characterize the aging grade. However, this may also be determined by the stability of the information. For RSD, it is necessary to capture the fluctuation expressed by the matrix in the earlier stages. The selection of a fusion scheme of different image features needs to consider the complementarity. In general, this paper provides a case study for matrix effect investigation and the utilization of plasma information for LIBS classification.

Data availability

Data underlying the results presented in this paper are not publicly available at this time because they are currently being used. However, they may be obtained from the authors upon reasonable request.

Conflicts of interest

There are no conflicts to declare.

Acknowledgements

This work was supported by the National Natural Science Foundation of China (U22B20119), the Foundation of Science and Technology Projects in Guangzhou (2025A04J7048), and the Fundamental Research Funds for the Central Universities (2022ZFJH004). We also acknowledge the support from the Guangdong Province Key Laboratory of Efficient and Clean Energy Utilization (2013A061401005).

References

1 M. Dong, J. Cai, S. Yao and J. Lu, *Application of LIBS for the Failure Characteristics Prediction of Heat-Resistant Steel*, John Wiley & Sons, 2023.
2 J. Wu, Y. Qiu, X. Li, H. Yu, Z. Zhang and A. Qiu, *J. Phys. D: Appl. Phys.*, 2020, **53**, 023001.
3 S. Pan, J. Lu, S. Yao, M. Jiang and P. Li, *Chin. J. Lasers*, 2010, **37**, 2126–2130.
4 Y. Dai, J. Li, W. Zhong, X. Dong, W. Li, S. Yao and J. Lu, *Acta Opt. Sin.*, 2014, **34**, 317–322.
5 J. Li, J. Lu, J. Li, S. Yao and M. Dong, *Chin. J. Lasers*, 2011, **38**, 233–238.
6 Y. Dai, X. Dong, W. Zhong, M. Dong, J. Lin, J. Li, S. Yao and J. Lu, *Chin. J. Lasers*, 2014, **41**, 269–274.
7 J. Li, J. Lu, Y. Dai, W. Zhong and S. Yao, *Appl. Surf. Sci.*, 2015, **346**, 302–310.
8 S. Lu, M. Dong, J. Huang, W. Li, J. Lu and J. Li, *Spectrochim. Acta, Part B*, 2018, **140**, 35–43.
9 J. Huang, M. Dong, S. Lu, W. Li, J. Lu, C. Liu and J. Yoo, *J. Anal. At. Spectrom.*, 2018, **33**, 720–729.
10 J. Huang, M. Dong, S. Lu, Y. Yu, C. Liu, J. Yoo and J. Lu, *Analyst*, 2019, **144**, 3736–3745.
11 S. Lu, S. Shen, J. Huang, M. Dong, J. Lu and W. Li, *Spectrochim. Acta, Part B*, 2018, **150**, 49–58.
12 Z. Shang, M. Dong, W. Li, J. Cai, K. Bai, F. Tang, Z. Li, S. Yao and J. Lu, *At. Spectrosc.*, 2024, **45**, 15–25.
13 Y. Zhang, M. Dong, J. Cai, H. Chen, C. Liu, J. Yoo and J. Lu, *J. Anal. At. Spectrom.*, 2022, **37**, 139–147.
14 Y. Zhang, M. Dong, J. Cai, W. Li and J. Lu, *Metall. Anal.*, 2020, **40**, 86–93.
15 J. Cai, M. Dong, Y. Zhang, Y. Chen, H. Chen, Y. Liang, W. Li and J. Lu, *At. Spectrosc.*, 2021, **42**, 43–50.
16 S. Lu, M. Dong, Q. Chen, J. Huang, Y. Yu and J. Lu, *Spectrochim. Acta, Part B*, 2019, **151**, 1–11.
17 Y. Fu, W. Guo, Z. Hou, S. Muhammed, T. Li, Y. Wang and Z. Wang, *Front. Phys.*, 2021, **16**, 1–10.
18 Y. Zhao, L. Zhang, J. Hou, W. Ma, L. Dong, W. Yin, L. Xiao, S. Jia and J. Yu, *Spectrochim. Acta, Part B*, 2019, **158**, 105644.
19 Y. Zhao, L. Zhang, S. Wang, J. Han, G. Xia, W. Ma, L. Dong, W. Yin, L. Xiao, S. Jia and J. Yu, *Spectrochim. Acta, Part B*, 2020, **173**, 105987.
20 H. Wu, C. Li, D. Wu, S. Liu, Z. Hu, C. Feng, R. Hai, F. Ding, G. Luo and H. Ding, *J. Anal. At. Spectrom.*, 2022, **37**, 2069–2081.
21 I. Schechter, V. Bulatov, L. Xu, V. Gridin and R. Krasniker, *J. Opt. Soc. Am.*, 2000, **SuD4**, 178–180.
22 Z. Ni, X. Chen, H. Fu, J. Wang and F. Dong, *Front. Phys.*, 2014, **9**, 439–445.
23 P. Zhang, L. Sun, H. Yu, P. Zeng, L. Qi and Y. Xin, *Anal. Chem.*, 2018, **90**, 4686–4694.
24 Q. Li, Y. Tian, B. Xue, N. Li, W. Ye, Y. Lu and R. Zheng, *J. Anal. At. Spectrom.*, 2020, **35**, 366–376.
25 Y. Zhang, Y. Lu, Y. Tian, Y. Li, W. Ye, J. Guo and R. Zheng, *Anal. Chim. Acta*, 2022, **1195**, 339423.
26 D. Zhang, Y. Chu, S. Ma, Z. Sheng, F. Chen, Z. Hu, S. Zhang, B. Wang and L. Guo, *Appl. Surf. Sci.*, 2020, **534**, 147601.
27 D. Zhang, Y. Chu, S. Ma, S. Zhang, H. Cui, Z. Hu, F. Chen, Z. Sheng, L. Guo and Y. Lu, *Anal. Chim. Acta*, 2020, **1107**, 14–22.
28 D. Zhang, Z. Chen, J. Nie, Y. Chu and L. Guo, *J. Anal. At. Spectrom.*, 2024, **39**, 2402.

29 G. Chen, P. Zheng, J. Wang, B. Li, X. Liu, Z. Yang, Z. Sun, H. Tian, D. Dong and L. Guo, *J. Anal. At. Spectrom.*, 2024, **39**, 1971.
30 D. Zhang, H. Ma, J. Nie, Y. Liu and L. Guo, *Talanta*, 2025, **281**, 126872.
31 D. Zhang, X. Niu, J. Nie, S. Shi, H. Ma and L. Guo, *Opt. Express*, 2024, **32**, 10851–10861.
32 F. Guan, Y. Liu, X. Niu, W. Huang, W. Li, P. Zheng, D. Zhang, G. Xun and L. Guo, *AP Nexus*, 2024, **3**, 066014.
33 J. Li and X. Liang, GBT 2039-1997 Metallic Materials-Creep and Stress-Rupture Test in Tension, *The State Bureau of Quality and Technical Supervision*, 1997.
34 Y. Li, *DL-T884-2004 Power Plant Metallography Inspection and Assessment Guide-Line*, China Electric Power Press, 2004.
35 R. Fisher, *Ann. Eugen.*, 1936, **7**, 179–188.
36 V. Baranov, O. Derkach, V. Grishina, M. Kanevskii and A. Sebrant, *Phys. Rev. E:Stat. Phys., Plasmas, Fluids, Relat. Interdiscip. Top.*, 1993, **8**, 1324.
37 P. Abhilasha, P. Prasad and R. Thareja, *Phys. Rev. E:Stat. Phys., Plasmas, Fluids, Relat. Interdiscip. Top.*, 1993, **48**, 2929.
38 C. Alvarez-Llamas, P. Purohit, J. Moros and J. Lasema, *Anal. Chem.*, 2022, **94**, 1840–1849.
39 Z. Liu, Y. Tian, Y. Lu, J. Guo, Y. Li, W. Ye and R. Zheng, *Spectrochim. Acta, Part B*, 2021, **180**, 106202.